



HAL
open science

Nanoscale Disorder Generates Subdiffusive Heat Transport in Self-Assembled Nanocrystal Films

James Utterback, Aditya Sood, Igor Coropceanu, Burak Guzelturk, Dmitri Talapin, Aaron Lindenberg, Naomi Ginsberg

► **To cite this version:**

James Utterback, Aditya Sood, Igor Coropceanu, Burak Guzelturk, Dmitri Talapin, et al.. Nanoscale Disorder Generates Subdiffusive Heat Transport in Self-Assembled Nanocrystal Films. *Nano Letters*, 2021, 21 (8), pp.3540-3547. 10.1021/acs.nanolett.1c00413 . hal-03513749

HAL Id: hal-03513749

<https://hal.science/hal-03513749>

Submitted on 3 Nov 2022

HAL is a multi-disciplinary open access archive for the deposit and dissemination of scientific research documents, whether they are published or not. The documents may come from teaching and research institutions in France or abroad, or from public or private research centers.

L'archive ouverte pluridisciplinaire **HAL**, est destinée au dépôt et à la diffusion de documents scientifiques de niveau recherche, publiés ou non, émanant des établissements d'enseignement et de recherche français ou étrangers, des laboratoires publics ou privés.

Nanoscale Disorder Generates Subdiffusive Heat Transport in Self-Assembled Nanocrystal Films

James K. Utterback,¹ Aditya Sood,² Igor Coropceanu,³ Burak Guzelturk,^{2,4,†} Dmitri V. Talapin,³ Aaron M. Lindenberg,^{2,4,5,6,7} Naomi S. Ginsberg^{1,8,9,10,11*}

¹ Department of Chemistry, University of California, Berkeley, California 94720, United States

² Stanford Institute for Materials and Energy Sciences, SLAC National Accelerator Laboratory, Menlo Park, California 94025, United States

³ Department of Chemistry and James Franck Institute, University of Chicago, Chicago, Illinois 60637, United States

⁴ Department of Materials Science and Engineering, Stanford University, Stanford, CA 94305, USA

⁵ The PULSE Institute for Ultrafast Energy Science, SLAC National Accelerator Laboratory, Menlo Park, California 94025, United States

⁶ Department of Photon Science, Stanford University, Menlo Park, California 94025, United States

⁷ SLAC National Accelerator Laboratory, Menlo Park, California 94025, United States

⁸ STROBE, National Science Foundation Science and Technology Center, University of California Berkeley, Berkeley, California 94720, United States

⁹ Department of Physics, University of California Berkeley, Berkeley, California 94720, United States

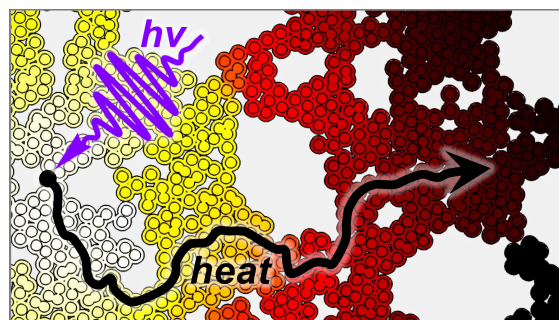
¹⁰ Materials Science Division and Molecular Biophysics and Integrated Bioimaging Division, Lawrence Berkeley National Laboratory, Berkeley, California 94720, United States

¹¹ Kavli Energy NanoSciences Institute at Berkeley, Berkeley, California 94720, United States

† Present Address: X-ray Science Division, Argonne National Laboratory, Lemont, IL 60439, USA

ABSTRACT

Investigating the impact of nanoscale heterogeneity on heat transport requires a spatiotemporal probe of temperature on the length and time scales intrinsic to heat navigating nanoscale defects. Here we use stroboscopic optical scattering microscopy to visualize nanoscale heat transport in disordered films of gold nanocrystals. We find that heat transport appears subdiffusive at the nanoscale. Finite element simulations show that tortuosity of the heat flow underlies the subdiffusive transport, owing to a distribution of nonconductive voids. Thus, while heat travels diffusively through contiguous regions of the film, the tortuosity causes heat to navigate circuitous pathways that make the observed mean-squared expansion of an initially localized temperature distribution appear subdiffusive on length scales comparable to the voids. Our approach should be broadly applicable to uncover the impact of both designed and unintended heterogeneities in a wide range of materials and devices that can affect more commonly used spatially-averaged thermal transport measurements.



At the nanoscale, heat flow must navigate length scales intrinsic to material heterogeneities.¹⁻⁷ This process contributes to the macroscopic thermal properties of a material but is typically aggregated into bulk parameters that can obfuscate microscopic origins. It is well known that, in the cases of electronic and mass transport, heterogeneity has impacts beyond a simple reduction in diffusivity, leading to fundamentally different transport regimes such as subdiffusive behavior.⁸⁻¹⁵ Subdiffusion refers to a mean-squared expansion of an initially localized heat distribution evolving as t^α , where $\alpha < 1$,^{16,17} such that the effective thermal conductivity falls off as a power law with the length scale traversed, tending to zero in the infinite limit.¹⁸ The ability to observe such behavior on the appropriate microscopic scales should therefore lead to mechanistic insights about the impact of defects on thermal transport.

The challenge of measuring nanoscale heat transport in heterogeneous media is that it requires a direct indicator of heat flow on the length and time scales of the encounters with nanoscale defects.^{1-7,19-24} Typically, thermal conductivity is measured on length scales orders of magnitude greater than the size of individual defects, yielding an average quantity. Ultrafast optical pump-probe measurements of thin films do not typically image heat spreading,²¹ and length-dependent steady-state thermal resistance measurements lack dynamical information and require constraining sample geometries and mechanical properties.²⁵ Although adequate in the limit that the scale measured far exceed those of material heterogeneities, the nanoscale heat transport properties, e.g., subdiffusion, may differ substantially from those obtained with typical measurements. Furthermore, the ability to obtain the combined spatial and temporal information required to establish relationships between nanoscale heterogeneity and nanoscale heat transport behavior has been lagging behind that of optical spatiotemporal techniques that probe electronic excited states in optoelectronic materials^{13,26-33} because their contrast mechanisms generally do not directly report on heat.

Here we take advantage of the unique ability of the recently developed³³ stroboscopic optical scattering microscopy (stoboSCAT) to spatiotemporally resolve nanoscale heat transport in films of colloidal Au nanocrystals (NCs). By virtue of its sensitivity to heat-induced local index of refraction changes, we resolve the expansion of a diffraction-limited heat pulse at room temperature with tens of nm and ~ 100 ps sensitivity. We find that heat transport in these NC films appears subdiffusive on the length and time scales of the measurement (100 ps – 100 ns and 30–300 nm). By simulating heat transport in geometries constructed to approximate transmission electron micrograph (TEM) images of similar NC films, we find that subdiffusion emerges mechanistically when voids are present in the films on scales within our sensitivity range. We learn that heat transport is locally diffusive on the small length scales between voids but that the voids lead to subdiffusive nanoscale heat transport by constraining heat flow along more protracted, circuitous paths. In fact, recasting the mean-squared expansion from direct space to a geodesic metric recovers diffusive behavior. At scales longer than the scale of voids, heat transport again appears diffusive but with a lower conductivity than is observed in the microscopic contiguous regions of the film. We anticipate that this recent ability to detect heat transport on the scale of heterogeneities will find use with a broad range of systems for which heat is expected to flow through both deliberately and unintentionally-introduced nanoscale heterogeneities, including both imperfect materials and phononic devices.^{34,35} It also illustrates the extent to which bulk transport can be improved by demonstrating the true nanoscale intrinsic limit of the diffusivity.

To experimentally monitor nanoscale heat transport in Au NC films, we use stoboSCAT microscopy. stoboSCAT is a recently developed time-resolved interferometric optical scattering microscopy that can track both electronic and thermal energy flow at the nanoscale.^{26,33,36-38}

strobeSCAT measures transient changes to a material's local optical polarizability induced by a focused ultrafast pump laser pulse (Figure 1).³³ These changes are measured by interferometrically detecting scattered probe light from the sample on a camera in wide-field and comparing it to a reference image taken in the absence of a pump pulse (Figure 1a).³³ In the Au NC films, the resulting differential image contrast maps the spatial distribution of heat in the sample, as reflected by the transient change of the scattering cross-section of the films.^{3,37,39–41} Its time evolution is determined by repeating the measurement with progressively longer pump-probe delays (Figure 1b). We report the signal as $\Delta R(r,t)/R$ since the experiment is performed in a reflection geometry, where the scattered light is detected at the field level via interference with light reflected from the substrate–sample interface.^{33,42,43}

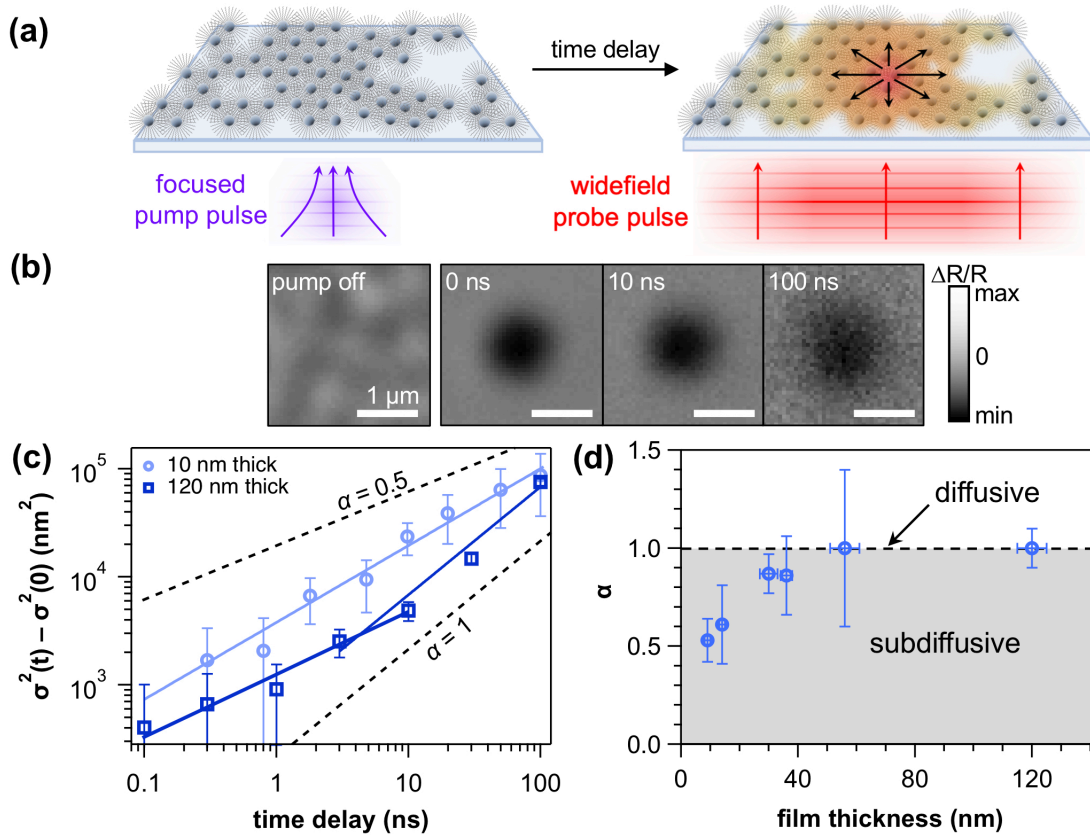


Figure 1. (a) Schematic of the strobeSCAT experiment, in which the sample is excited with a focused pump light pulse and then the subsequent heat diffusion is imaged using a wide-field probe pulse after a controlled time delay. (b) Representative ground-state scattering image (pump off) and strobeSCAT time series on a 120 nm thick region of a film of 4.4 nm Au NCs with DDT ligands. (c) Representative mean-squared expansion curves of thin and thick regions of two different 4.4 nm Au–DDT films. The mean-squared expansion curve of a 10 nm thick region is fit to give a single value of α of 0.7 ± 0.1 . A 120 nm thick region of an identically-prepared film is fit over 0.1–10 ns to give $\alpha = 0.6 \pm 0.1$ and separately over the 3–100 ns to give $\alpha = 1.0 \pm 0.1$. (d) Thickness dependence of α for different regions of a single 4.4 nm Au–DDT film, where α was fit over the 1–100 ns in each case. The subdiffusive regime ($\alpha < 1$) is shaded grey, and the diffusive regime ($\alpha = 1$) is indicated with a dashed line. See raw data in Figure S2a.

Specifically, films of 4.4 nm diameter Au NCs capped with dodecanethiol (DDT) ligands were dropcast onto glass slides from a colloidal solution (Figure S1, Methods). We illuminate the Au NC film at room temperature with a 405 nm pump light pulse (~ 100 ps), focused to a spot size with a full-width at half maximum (FWHM) of 590 nm (Figure 1a). The electrons excited at the d–s interband transition rapidly equilibrate with the lattice via electron–phonon coupling within the NCs within the duration of the pulse,³⁷ and we visualize the time-dependent optical scattering profile of the resulting heat distribution with a wide-field 635 nm wavelength probe light pulse, detuned from the plasmon resonance peak at 514 nm, over a 0.1–100 ns time window (Figure 1a). With a 2σ -integrated excitation fluence of $\sim 9 \mu\text{J}/\text{cm}^2$, we estimate an average initial change in temperature on the order of a few Kelvin.³⁷ The region of elevated temperature appears as negative (dark) contrast (Figure 1b).^{3,40,41} By taking an azimuthal average of the spatial distribution of the transient scattering profile and fitting to a Gaussian function, we monitor in-plane heat diffusion, quantified by the mean-squared expansion, $\sigma^2(t) - \sigma^2(0)$, with a few tens of nm spatial sensitivity that is determined by the signal-to-noise ratio rather than the diffraction limit (Figure 1c). We observe an associated root-mean-squared expansion of the heat profile from ~ 30 out to ~ 300 nm depending on the region interrogated in the film, corresponding to a range of 4 to 40 NC–NC center-to-center distances (Figure 1c, S2).

Our measurements point to subdiffusive heat transport in the colloidal NC films over a substantial portion of the three orders of magnitude of time delays considered. Figure 1c shows representative mean-squared expansion curves collected in thin and thick regions of two identically-prepared films (see Figure S2 for all curves). Fitting each data set to $\sigma^2(t) - \sigma^2(0) \propto t^\alpha$ yields different values of the exponent α in different regions of the film (Figure 1d, S2). In many regions, we find $\alpha < 1$, suggesting subdiffusion. The exponent α increases with film thickness, as determined by atomic force microscopy correlated to the same region of a film probed with stroboSCAT (Figure S3), starting from 0.53 at a thickness of 9 nm up to ~ 1 for a 120-nm-thick film (Figure 1d). α also varies over the time window measured in some locations in the film. For example, in the 120-nm-thick region of the 4.4 nm NC film in Figure 1c the slope of the mean-squared expansion on the log-log plot appears to increase with time, becoming approximately diffusive after ~ 10 ns, and was therefore fit piecewise. Around this time delay, we observe root-mean-squared expansions of ~ 40 – 140 nm, depending on the film thickness. The expansion during the diffusive time window of the 120-nm-thick film corresponds to a heat diffusion coefficient of $(3.0 \pm 0.2) \times 10^{-3} \text{ cm}^2 \text{ s}^{-1}$, or thermal conductivity of approximately $0.3 \text{ W m}^{-1} \text{ K}^{-1}$, similar to a previous study of analogous NC films (see Supporting Information).⁵⁰ Subdiffusive transport behavior is consistently observed in multiple films and over multiple regions within each one (Figures 1c,d and S2) and does not strongly depend on NC size—a film of 5.7 nm NCs exhibit analogous behavior to the 4.4 nm NC film (Figure S2)—which is consistent with macroscopic thermal conductivity measurements.³³ Finally, in contrast to the subdiffusive behavior observed in the colloidal NC films, identical stroboSCAT measurements on a ~ 6 nm thick continuous polycrystalline Au film show normal diffusion with $\alpha = 1.0 \pm 0.1$, a diffusion coefficient of $(1.1 \pm 0.1) \times 10^{-1} \text{ cm}^2 \text{ s}^{-1}$ and thermal conductivity of $27 \pm 2 \text{ W m}^{-1} \text{ K}^{-1}$ (Figure S4).

We hypothesize that the subdiffusive behavior in these NC films originates from spatial disorder in the NC packing that forces heat to navigate a geometrically-restricted environment induced by voids. While the nanoscale heterogeneities themselves are not directly resolved by the optical scattering technique, we support this correlation between subdiffusive behavior and the presence of voids below with the combination of the film thickness dependence of α (Figure 1d), heat transport simulations based on TEM images of a NC film (Figure 2a), and the normal diffusive

behavior observed in polycrystalline Au (Figure S4). Specifically, the TEM image of an incomplete monolayer of 5.7 nm Au–DDT NCs (Figure 2a) shows voids on length scales ranging from single NC vacancies to a few hundreds of nm. 4.4 nm NCs exhibit packing behavior that is qualitatively similar to that of the 5.7 nm NCs in Figure 2a. While NCs may self-assemble on the surfaces of the glass slides used for stroboSCAT experiments differently than they do on carbon TEM grids, it is reasonable to expect that the NC films in the stroboSCAT experiments have similar structure to that in Figure 2a.^{44–46} Even in multilayer regions of a film on TEM grids, similar voids are apparent (Figure S5), suggesting a likeness especially to thinner regions of the film. The below analysis suggests that normal diffusion occurs in the moderately well-packed regions and that the subdiffusion stems from heat having to circumnavigate the voids.

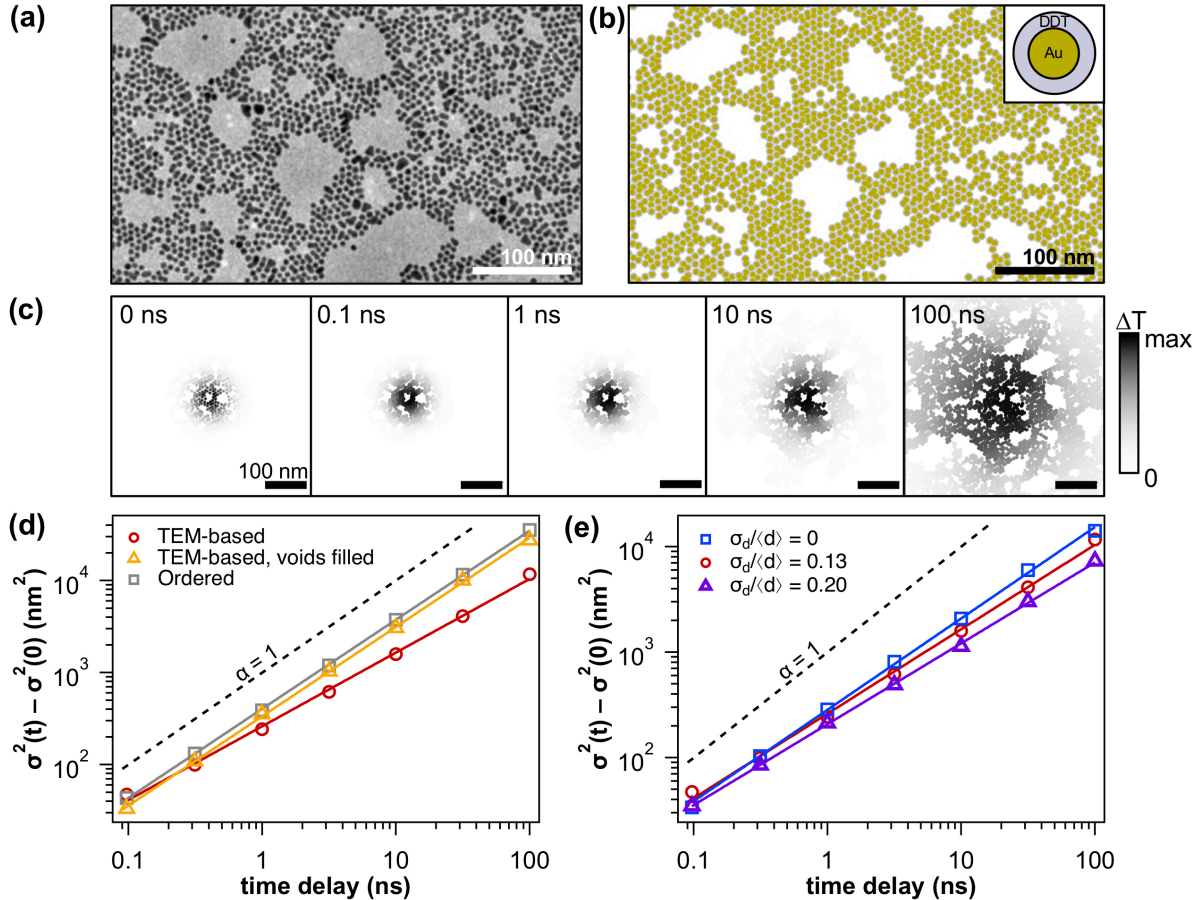


Figure 2. (a) Representative TEM image of 5.7 nm Au–DDT film on which simulation geometries are based. (b) Simulation geometry with voids present and 13% inter-NC separation disorder ($\sigma_d/\langle d \rangle$). (c) Simulated temperature map time series for NC array from (b). (d) Mean-squared expansion curves comparing simulations of the geometry based on TEM image of Figure 2a with voids and $\sigma_d/\langle d \rangle = 13\%$ (red circles), the same geometry but with the voids filled in with ligand material (orange triangles), and an ordered NC array without voids and $\sigma_d/\langle d \rangle = 0$ (grey squares). Corresponding temperature map time series appear in Figure S7. The heat diffusion coefficients, D , for the ligand-filled void (orange triangles) and perfectly ordered (grey squares) geometries, determined by fitting to $\sigma^2(t) - \sigma^2(0) = 2Dt$, are 1.7 and $1.9 \times 10^{-3} \text{ cm}^2 \text{ s}^{-1}$, respectively. (e) Mean-squared expansion curves comparing simulations of the geometry with voids based on TEM image of Figure 2a for $\sigma_d/\langle d \rangle = 0\%$, 13% and 20% .

To test the hypothesis that voids can give rise to the experimentally observed subdiffusive behavior, we carry out finite element heat transport simulations in a disordered Au–DDT NC composite film (Figure 2b, S5) that approximates the experimental condition in the TEM image of Figure 2a. Simulations are initialized using a Gaussian profile (FWHM = 76 nm) of elevated temperature with a peak deviation from the background of $\Delta T = 1$ K in the Au NC cores (Figure S7), reflecting the stroboSCAT experiments within the constraints of simulation tractability (see below). Fourier’s equation is solved as a function of space and time to map the heat expansion subject to the boundary conditions dictated by the nonconductive voids and the NC–ligand interfacial resistance (Figure 2b, Methods). Figure 2c shows how the simulated temperature profile expands over time from 0 to 100 ns in the TEM-inspired film configuration with local spatial disorder and voids. Consistent with ultrafast electron diffraction observations,³⁷ on the shortest timescales beneath our experimental time resolution (~ 100 ps), heat transport is virtually instantaneous within the NC cores and transfers across the NC–ligand interface such that the subsequent evolution is limited by the relatively slow conduction in the ligand material (Figure S8). As heat flows around the voids over 100 ps – 100 ns, the profile develops anisotropy. Mimicking the stroboSCAT analysis, the temperature profiles are azimuthally averaged and then fit to a Gaussian function to obtain the mean-squared expansion (Figure 2d), revealing a subdiffusive exponent of $\alpha = 0.80$ (Figure 2d, red).

Interestingly, filling the voids with ligand material (Figure S6 and S7), recovers the diffusive behavior with near-unity α , despite the disorder in the NC positions (Figure 2d, orange). Both this result and a simulation on a perfectly ordered hexagonal lattice without voids (Figure 2d, grey) yield $\alpha = 0.98$, differing only slightly in their diffusion coefficients, likely due to the reduced volume fraction of the highly conductive Au. Note that the deviation between these results and $\alpha = 1$ is likely noise due to a combination of factors, such as simulation tolerance, resolution, and fitting, and provides an estimate of the magnitude of the uncertainty in the approach. Small increases or decreases to the inter-NC separation disorder (Figure S6 and S7), characterized by $\sigma_d/\langle d \rangle$, the separation’s standard deviation normalized to its mean, introduce small changes to the resulting α , increasing from 0.80 for 13% disorder to 0.87 for 0% disorder (Figure 2e, blue) and decreasing to 0.76 for 20% disorder (Figure 2e, purple). This tuning of the extent of subdiffusivity can be rationalized in terms of the relative number and size of voids that disrupt the local connectivity in the film (Figure S6). Our findings suggest that even though dense regions of a NC solid can display essentially crystalline local order even in submonolayer regions of a film (Figure S5b), subdiffusive transport can still occur on scales comparable to any voids.

The resemblance between the simulated subdiffusive heat transport and the experimental stroboSCAT data suggests that the simulations capture the essential underlying physics. The value of α in the TEM image-based simulation geometry lies roughly in the middle of the range of experimental values found in different regions of the dropcast NC films. The precise value of α depends on the local NC packing order (Figure 2e), and likely also on the size distribution and arrangement of voids, which can feasibly change in different films and different regions of the same film. Additionally, the size of the simulation geometry and consequently the initial temperature distribution size were limited by computational power. Separately, the magnitude of the mean-squared expansion found in the simulations underestimates those of the experiments by a factor of 1–20, with the largest deviations occurring at early times. This quantitative discrepancy could be due to the impact of the inherently 3D geometry of the films measured in experiments, the interaction with the glass substrate altering the experimentally observed mean-squared expansion, or overestimates of the ligand thermal or density parameters employed in the

simulations (Methods), due, for example, to ligand coverage.⁴⁷ In addition, our simple model does not account for the possibility of ballistic phonon/electron transport within NC cores or between NC cores that are in direct contact, which could enhance the transport over small distances at early times in particular.⁴⁸

To further validate our void-induced subdiffusivity hypothesis, we compare the simulated temperature map to a map of geodesic distances in the simulated film and show that diffusive transport is recovered in geodesic space. The geodesic distance (ℓ_{\min}) between two points is the length of the shortest path between them through contiguous material (i.e., in the solid phase, avoiding voids).⁴⁹ Figure 3 compares a contour map of the geodesic distance from the central NC (Figure 3a) to a contour map of the temperature after 100 ns of evolution (Figure 3b), using the geometry of Figure 2b (Figure S9). The initial condition used in this simulation elevates the temperature of the central NC alone (Figure S7e). Moving out from the center, voids disrupt the path connectivity, making the shortest, geodesic distance one that curves to circumnavigate voids. The boxed regions in Figure 3a show representative locations where contours curve radially inward on the more radially distant sides of voids, resulting in notable increases in ℓ_{\min} relative to the radial distance r from the central NC. The temperature map at 100 ns (Figure 3b) bears a strong resemblance to the geodesic map (Figure 3a) in that temperature contours curve radially inwards on the more radially distant sides of voids (boxed regions of Figure 3b). In fact, plotting the mean-squared expansion along the geodesic coordinate as a function of time, $\langle \ell_{\min}^2(t) \rangle$,⁴⁹ recovers the diffusive behavior, with $\alpha = 0.99$ (Figure 3c, Figure S9). Additional correlations between local void area fraction, local geodesic distance and the “instantaneous” exponent $\alpha(t)$ appear in Figure S9 and S10 and associated text.

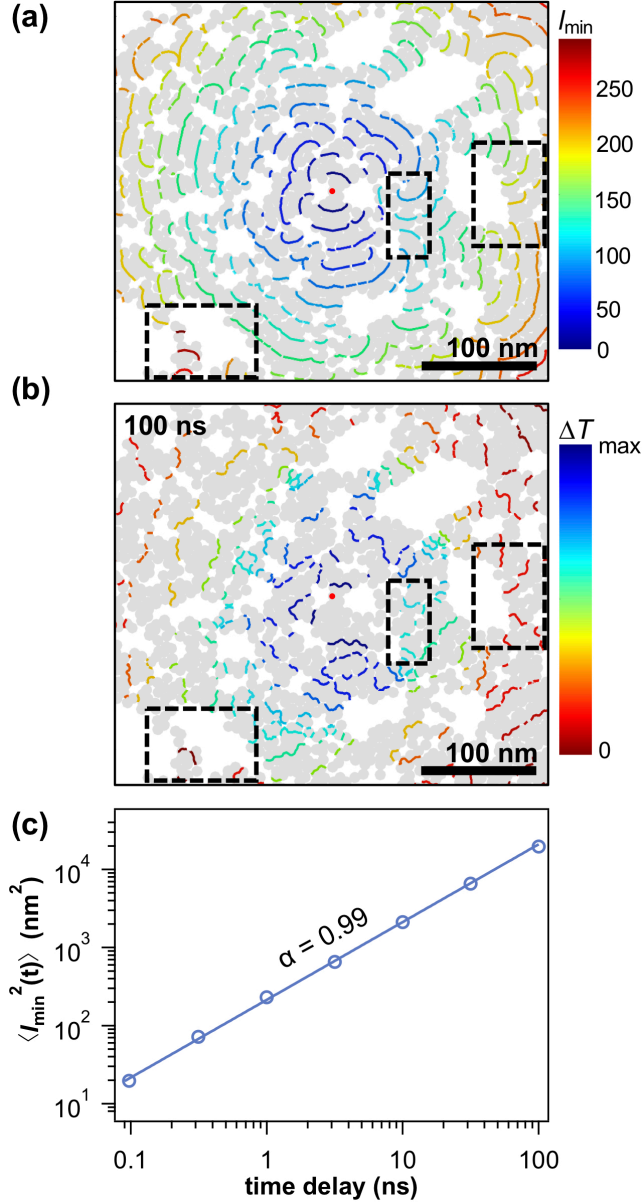


Figure 3. (a) Contour maps of the geodesic distance from the central NC in nm and (b) the temperature 100 ns after raising the temperature of the central NC by $\Delta T = 1$ K for the same simulation landscape as Figure 2. The central NC core is indicated with a red dot. (c) Log-log plot of the mean-squared expansion along the geodesic distance as a function of time, $\langle l_{\min}^2(t) \rangle$, for the same simulation.

Altogether, the observation that we recover diffusive behavior in geodesic space suggests that the voids are responsible for the nanoscale subdiffusive heat expansion measured in Euclidean space. Conceptually, radial heat expansion slows down as it wraps around the voids, actually moving over a distance of l_{\min} rather than r . Thus, while locally heat flows diffusively according to the heat diffusion equation through contiguous regions of the film, the boundary conditions imparted by the voids cause heat to navigate circuitous pathways that make the observed mean-squared expansion subdiffusive on the scale of the voids. On scales distinctly smaller (Figure 3c) or larger (Figure 1c) than voids, diffusive behavior is still observed.

While subdiffusive transport is observed routinely in spatiotemporal nanoscale electronic transport measurements,^{11–14} stroboSCAT's contrast mechanism and spatiotemporal nature have allowed us to observe heat subdiffusion, with sensitivity on the length and time scales on which the temperature gradient encounters defects. We explore the implications of having this new information below, both by placing the nanoscale observations into the broader context of a larger dynamic range of scales and dimensionality and by describing how the nanoscale observations impact our interpretation of bulk properties. We furthermore speculate on how this information could be used to control energy flow in materials at all scales.

Our experiments indicate that in the NC films studied here, the apparent thermal conductivity is scale-dependent over the few- to hundreds-of-nm-sized voids, which motivates a discussion relating the observed properties across scales. The highest thermal conductivity is observed at the shortest length and time scales,³⁷ reflecting transport in the most completely/densely packed regions of the film. As the initially localized heat distributions continue to expand and the scale of the mean squared expansion becomes comparable to those of voids, the expansion rate progressively decreases.³⁷ On length scales significantly larger than those of the heterogeneities, transport returns to a diffusive regime, as observed in the thicker regions of our films (Figure 1c). Such length-dependent thermal conductivity has been predicted theoretically for subdiffusive systems.^{16,18} Interestingly, previous measurements of thermal conductivity in similar Au–DDT NC films fashioned into superlattices found no thickness dependence for films as thin as ~30 nm,⁵⁰ implying normal diffusion; we find a length scale of a few tens of nm to be the transition threshold between subdiffusive and normal transport regimes in our films (Figure 1). Our results suggest that the importance of subdiffusive transport and associated heterogeneity is greatest for lower-dimensional materials since material connectivity increases with dimension.^{44–46} In other words, voids present a greater obstacle to transport when the heat flow cannot detour by traveling around a void in an orthogonal dimension.

We suspect that subdiffusive heat transport at the nanoscale may be a common phenomenon in systems with nanoscale heterogeneity. A macroscopic measurement of such a system would average over the impact of the heterogeneities and yield a conductivity smaller than that which could be achieved in the absence of the heterogeneity.^{7,18,37} By virtue of revealing the relationship between variations in structure to variations in transport, nanoscale thermal conductivity measurements should be valuable to rationalize and improve the bulk thermal properties of materials: the extent to which nanoscale measurements reveal anomalous diffusion and the scales on which it occurs can provide important microscopic information on the origins of suboptimal conduction at larger scales. For example, the distribution of sizes, shapes, and locations of voids could potentially lead to different transport behaviors associated with their characteristic scales that impact macroscopic flow in various ways.^{15,49}

The nanoscale structure–function relationships that we have shown can pave the way to conceptualizing and designing subdiffusive heat transport in a range of systems beyond NC arrays, such as low-dimensional nanostructures and amorphous polymers.^{25,51} Because the mechanism of nanoscale subdiffusive heat transport found here is geometric in nature, it could apply wherever heat must navigate indirect pathways. For example, this picture could explain the subdiffusive transport inferred in planar π -conjugated molecular nanoribbons, provided that defects in the single crystalline structure were imposing transport barriers to circumnavigate.²⁵ Furthermore, in bulk amorphous polymers, where thermal conductivity is strongly suppressed compared to that in individual molecular chains due to the tortuous path taken by thermal vibrations, it would be

interesting to explore whether heat transmits subdiffusively.⁵¹ Tortuosity-based design principles for heat management could be intentionally leveraged,³⁴ for example, to control the path of heat flow, or to tailor heat flow over specific length scales.

We have presented an observation of, and a mechanistic model for, nanoscale subdiffusive heat transport in composite Au NC–ligand films. Together, the experiments and simulations demonstrate that subdiffusive heat transport can occur at the scale of realistic voids in disordered nanoparticle solids, and we suggest that it is likely to occur in other materials with similar heterogeneities. Locally, heat travels diffusively in contiguous regions of the film, but tortuosity makes the transport subdiffusive on length scales of the voids. Beyond heat transport, the nature of the heterogeneity studied here would lead to subdiffusive electronic or mass transport as well, which could also be captured using stroboSCAT, either separately or in combination. Furthermore, stroboSCAT could be used to map nanoscale heat flow in a wide range of systems, potentially revealing the role of defects and heterogeneities, and also enabling realistic comparison of transport in deliberately nanostructured or microstructured devices with performance anticipated by their ideal design. Moreover, combined with temperature calibration, this approach could be adapted to construct absolute temperature maps of high interest for far-from-equilibrium thermodynamics studies at the nanoscale.

Present Addresses

†X-ray Science Division, Argonne National Laboratory, Lemont, IL 60439, USA

Notes

The authors declare no competing financial interest.

ACKNOWLEDGMENTS

We acknowledge H. L. Weaver, J. G. Raybin and J. C. Portner for helpful discussions. This work, including all stroboSCAT measurements and interpretation were primarily funded through the “Photonics at Thermodynamic Limits” Energy Frontier Research Center funded by the U.S. Department of Energy, Office of Science, Office of Basic Energy Sciences, under Award Number DE-SC0019140. Data interpretation was also supported by the SIMES Institute for Energy Sciences from the Department of Energy, Office of Science, Basic Energy Sciences, Materials Sciences and Engineering Division, under Contract DE-AC02-76SF00515. Sample preparation and characterization were supported by the Office of Basic Energy Sciences, the U.S. Department of Energy, under Award No. DE-SC0019375. Simulations were performed in the Molecular Graphics and Computation Facility, College of Chemistry, UC Berkeley which is funded by NIH S10OD023532. J.K.U. acknowledges support from the Camille and Henry Dreyfus Foundation’s Postdoctoral Program in Environmental Chemistry (data collection and initial simulations), and the Arnold O. Beckman Postdoctoral Fellowship in Chemical Sciences from the Arnold and Mabel Beckman Foundation (manuscript preparation). N.S.G. and D.V.T. also acknowledge Alfred P. Sloan Research Fellowships, David and Lucile Packard Foundation Fellowships for Science and Engineering, and Camille and Henry Dreyfus Teacher-Scholar Awards.

REFERENCES

- (1) Yang, N.; Xu, X.; Zhang, G.; Li, B. Thermal Transport in Nanostructures. *AIP Adv.* **2012**, *2* (4), 041410. <https://doi.org/10.1063/1.4773462>.
- (2) Minnich, A. J.; Johnson, J. A.; Schmidt, A. J.; Esfarjani, K.; Dresselhaus, M. S.; Nelson, K. A.; Chen, G. Thermal Conductivity Spectroscopy Technique to Measure Phonon Mean Free Paths. *Phys. Rev. Lett.* **2011**, *107* (9). <https://doi.org/10.1103/PhysRevLett.107.095901>.
- (3) Block, A.; Liebel, M.; Yu, R.; Spector, M.; Sivan, Y.; Abajo, F. J. G. de; Hulst, N. F. van. Tracking Ultrafast Hot-Electron Diffusion in Space and Time by Ultrafast Thermomodulation Microscopy. *Sci. Adv.* **2019**, *5* (5), No. eaav8965. <https://doi.org/10.1126/sciadv.aav8965>.
- (4) Frazer, T. D.; Knobloch, J. L.; Hoogeboom-Pot, K. M.; Nardi, D.; Chao, W.; Falcone, R. W.; Murnane, M. M.; Kapteyn, H. C.; Hernandez-Charpak, J. N. Engineering Nanoscale Thermal Transport: Size- and Spacing-Dependent Cooling of Nanostructures. *Phys. Rev. Appl.* **2019**, *11* (2), 024042. <https://doi.org/10.1103/PhysRevApplied.11.024042>.
- (5) Karl, R. M.; Mancini, G. F.; Knobloch, J. L.; Frazer, T. D.; Hernandez-Charpak, J. N.; Abad, B.; Gardner, D. F.; Shanblatt, E. R.; Tanksalvala, M.; Porter, C. L.; Bevis, C. S.; Adams, D. E.; Kapteyn, H. C.; Murnane, M. M. Full-Field Imaging of Thermal and Acoustic Dynamics in an Individual Nanostructure Using Tabletop High Harmonic Beams. *Sci. Adv.* **2018**, *4* (10), No. eaau4295. <https://doi.org/10.1126/sciadv.aau4295>.
- (6) Xiong, K.; Liu, Z. Temperature Dependence of Heat Conduction Coefficient in Nanotube/Nanowire Networks. *Chin. Phys. B* **2017**, *26* (9), 098904. <https://doi.org/10.1088/1674-1056/26/9/098904>.
- (7) Olson, D. H.; Avincola, V. A.; Parker, C. G.; Braun, J. L.; Gaskins, J. T.; Tomko, J. A.; Opila, E. J.; Hopkins, P. E. Anisotropic Thermal Conductivity Tensor of β -Y₂Si₂O₇ for Orientational Control of Heat Flow on Micrometer Scales. *Acta Mater.* **2020**, *189*, 299–305. <https://doi.org/10.1016/j.actamat.2020.02.040>.
- (8) Alonso, D.; Ruiz, A.; de Vega, I. Polygonal Billiards and Transport: Diffusion and Heat Conduction. *Phys. Rev. E* **2002**, *66* (6), 066131. <https://doi.org/10.1103/PhysRevE.66.066131>.
- (9) Alonso, D.; Ruiz, A.; de Vega, I. Transport in Polygonal Billiards. *Phys. Nonlinear Phenom.* **2004**, *187* (1–4), 184–199. <https://doi.org/10.1016/j.physd.2003.09.007>.
- (10) Montroll, E. W.; Scher, H. Random Walks on Lattices. IV. Continuous-Time Walks and Influence of Absorbing Boundaries. *J. Stat. Phys.* **1973**, *9* (2), 101–135. <https://doi.org/10.1007/BF01016843>.
- (11) Scher, H.; Lax, M. Stochastic Transport in a Disordered Solid. II. Impurity Conduction. *Phys. Rev. B* **1973**, *7* (10), 4502–4519. <https://doi.org/10.1103/PhysRevB.7.4502>.
- (12) Gu, Q.; Schiff, E. A.; Grebner, S.; Wang, F.; Schwarz, R. Non-Gaussian Transport Measurements and the Einstein Relation in Amorphous Silicon. *Phys. Rev. Lett.* **1996**, *76* (17), 3196–3199. <https://doi.org/10.1103/PhysRevLett.76.3196>.
- (13) Akselrod, G. M.; Prins, F.; Poulidakos, L. V.; Lee, E. M. Y.; Weidman, M. C.; Mork, A. J.; Willard, A. P.; Bulović, V.; Tisdale, W. A. Subdiffusive Exciton Transport in Quantum Dot Solids. *Nano Lett.* **2014**, *14* (6), 3556–3562. <https://doi.org/10.1021/nl501190s>.
- (14) Lee, E. M. Y.; Tisdale, W. A.; Willard, A. P. Can Disorder Enhance Incoherent Exciton Diffusion? *J. Phys. Chem. B* **2015**, *119* (30), 9501–9509. <https://doi.org/10.1021/acs.jpcc.5b01886>.

- (15) Chen, L.; Deem, M. W. Two-Dimensional Diffusion in the Presence of Topological Disorder. *Phys. Rev. E* **2003**, *68* (2), 021107. <https://doi.org/10.1103/PhysRevE.68.021107>.
- (16) Bouchaud, J.-P.; Georges, A. Anomalous Diffusion in Disordered Media: Statistical Mechanisms, Models and Physical Applications. *Phys. Rep.* **1990**, *195* (4), 127–293. [https://doi.org/10.1016/0370-1573\(90\)90099-N](https://doi.org/10.1016/0370-1573(90)90099-N).
- (17) Metzler, R.; Klafter, J. The Random Walk's Guide to Anomalous Diffusion: A Fractional Dynamics Approach. *Phys. Rep.* **2000**, *339* (1), 1–77. [https://doi.org/10.1016/S0370-1573\(00\)00070-3](https://doi.org/10.1016/S0370-1573(00)00070-3).
- (18) Li, B.; Wang, J. Anomalous Heat Conduction and Anomalous Diffusion in One-Dimensional Systems. *Phys. Rev. Lett.* **2003**, *91* (4), 044301. <https://doi.org/10.1103/PhysRevLett.91.044301>.
- (19) Sood, A.; Cheaito, R.; Bai, T.; Kwon, H.; Wang, Y.; Li, C.; Yates, L.; Bougher, T.; Graham, S.; Asheghi, M.; Goorsky, M.; Goodson, K. E. Direct Visualization of Thermal Conductivity Suppression Due to Enhanced Phonon Scattering Near Individual Grain Boundaries. *Nano Lett.* **2018**, *18* (6), 3466–3472. <https://doi.org/10.1021/acs.nanolett.8b00534>.
- (20) Sood, A.; Xiong, F.; Chen, S.; Wang, H.; Selli, D.; Zhang, J.; McClellan, C. J.; Sun, J.; Donadio, D.; Cui, Y.; Pop, E.; Goodson, K. E. An Electrochemical Thermal Transistor. *Nat. Commun.* **2018**, *9* (1), 4510. <https://doi.org/10.1038/s41467-018-06760-7>.
- (21) Olson, D. H.; Braun, J. L.; Hopkins, P. E. Spatially Resolved Thermoreflectance Techniques for Thermal Conductivity Measurements from the Nanoscale to the Mesoscale. *J. Appl. Phys.* **2019**, *126* (15), 150901. <https://doi.org/10.1063/1.5120310>.
- (22) Wang, D.; Koh, Y. R.; Kudyshev, Z. A.; Maize, K.; Kildishev, A. V.; Boltasseva, A.; Shalaev, V. M.; Shakouri, A. Spatial and Temporal Nanoscale Plasmonic Heating Quantified by Thermoreflectance. *Nano Lett.* **2019**, *19* (6), 3796–3803. <https://doi.org/10.1021/acs.nanolett.9b00940>.
- (23) Hartland, G. V. Optical Studies of Dynamics in Noble Metal Nanostructures. *Chem. Rev.* **2011**, *111* (6), 3858–3887. <https://doi.org/10.1021/cr1002547>.
- (24) Pavlidis, G.; Hilton, A. M.; Brown, J. L.; Heller, E. R.; Graham, S. Monitoring the Joule Heating Profile of GaN/SiC High Electron Mobility Transistors via Cross-Sectional Thermal Imaging. *J. Appl. Phys.* **2020**, *128* (7), 075705. <https://doi.org/10.1063/5.0014407>.
- (25) Tang, H.; Xiong, Y.; Zu, F.; Zhao, Y.; Wang, X.; Fu, Q.; Jie, J.; Yang, J.; Xu, D. Length-Dependent Thermal Transport in One-Dimensional Self-Assembly of Planar π -Conjugated Molecules. *Nanoscale* **2016**, *8* (23), 11932–11939. <https://doi.org/10.1039/C5NR09043A>.
- (26) Ginsberg, N. S.; Tisdale, W. A. Spatially Resolved Photogenerated Exciton and Charge Transport in Emerging Semiconductors. *Annu. Rev. Phys. Chem.* **2020**, *71* (1), 1–30. <https://doi.org/10.1146/annurev-physchem-052516-050703>.
- (27) Akselrod, G. M.; Deotare, P. B.; Thompson, N. J.; Lee, J.; Tisdale, W. A.; Baldo, M. A.; Menon, V. M.; Bulović, V. Visualization of Exciton Transport in Ordered and Disordered Molecular Solids. *Nat. Commun.* **2014**, *5* (1), 3646. <https://doi.org/10.1038/ncomms4646>.
- (28) Wan, Y.; Guo, Z.; Zhu, T.; Yan, S.; Johnson, J.; Huang, L. Cooperative Singlet and Triplet Exciton Transport in Tetracene Crystals Visualized by Ultrafast Microscopy. *Nat. Chem.* **2015**, *7* (10), 785–792. <https://doi.org/10.1038/nchem.2348>.
- (29) Yuan, L.; Wang, T.; Zhu, T.; Zhou, M.; Huang, L. Exciton Dynamics, Transport, and Annihilation in Atomically Thin Two-Dimensional Semiconductors. *J. Phys. Chem. Lett.* **2017**, *8* (14), 3371–3379. <https://doi.org/10.1021/acs.jpcclett.7b00885>.

- (30) Kennedy, C. L.; Hill, A. H.; Massaro, E. S.; Grumstrup, E. M. Ultrafast Excited-State Transport and Decay Dynamics in Cesium Lead Mixed Halide Perovskites. *ACS Energy Lett.* **2017**, *2* (7), 1501–1506. <https://doi.org/10.1021/acsenergylett.7b00257>.
- (31) Penwell, S. B.; Ginsberg, L. D. S.; Noriega, R.; Ginsberg, N. S. Resolving Ultrafast Exciton Migration in Organic Solids at the Nanoscale. *Nat. Mater.* **2017**, *16* (11), 1136–1141. <https://doi.org/10.1038/nmat4975>.
- (32) Zhu, T.; Snaider, J. M.; Yuan, L.; Huang, L. Ultrafast Dynamic Microscopy of Carrier and Exciton Transport. *Annu. Rev. Phys. Chem.* **2019**, *70* (1), 219–244. <https://doi.org/10.1146/annurev-physchem-042018-052605>.
- (33) Delor, M.; Weaver, H. L.; Yu, Q.; Ginsberg, N. S. Imaging Material Functionality through Three-Dimensional Nanoscale Tracking of Energy Flow. *Nat. Mater.* **2020**, *19* (1), 56–62. <https://doi.org/10.1038/s41563-019-0498-x>.
- (34) Chavez, R.; Angst, S.; Maize, K.; Gondorf, A.; Schierner, G.; Wolf, D. E.; Lorke, A.; Shakouri, A. Thermoreflectance Imaging of Percolation Effects and Dynamic Resistance in Indium Tin Oxide Nanoparticle Layers. *J. Appl. Phys.* **2012**, *112* (8), 083705. <https://doi.org/10.1063/1.4757960>.
- (35) Yazdani, N.; Jansen, M.; Bozyigit, D.; Lin, W. M. M.; Volk, S.; Yarema, O.; Yarema, M.; Juranyi, F.; Huber, S. D.; Wood, V. Nanocrystal Superlattices as Phonon-Engineered Solids and Acoustic Metamaterials. *Nat. Commun.* **2019**, *10* (1), 4236. <https://doi.org/10.1038/s41467-019-12305-3>.
- (36) Delor, M.; Slavney, A. H.; Wolf, N. R.; Filip, M. R.; Neaton, J. B.; Karunadasa, H. I.; Ginsberg, N. S. Carrier Diffusion Lengths Exceeding 1 Mm Despite Trap-Limited Transport in Halide Double Perovskites. *ACS Energy Lett.* **2020**, *5* (5), 1337–1345. <https://doi.org/10.1021/acsenergylett.0c00414>.
- (37) Guzelturk, B.; Utterback, J. K.; Coropceanu, I.; Kamysbayev, V.; Janke, E. M.; Zajac, M.; Yazdani, N.; Cotts, B. L.; Park, S.; Sood, A.; Lin, M.-F.; Reid, A. H.; Kozina, M. E.; Shen, X.; Weathersby, S. P.; Wood, V.; Salleo, A.; Wang, X.; Talapin, D. V.; Ginsberg, N. S.; Lindenberg, A. M. Nonequilibrium Thermodynamics of Colloidal Gold Nanocrystals Monitored by Ultrafast Electron Diffraction and Optical Scattering Microscopy. *ACS Nano* **2020**, *14* (4), 4792–4804. <https://doi.org/10.1021/acsnano.0c00673>.
- (38) Folie, B. D.; Tan, J. A.; Huang, J.; Sercel, P. C.; Delor, M.; Lai, M.; Lyons, J. L.; Bernstein, N.; Efros, A. L.; Yang, P.; Ginsberg, N. S. Effect of Anisotropic Confinement on Electronic Structure and Dynamics of Band Edge Excitons in Inorganic Perovskite Nanowires. *J. Phys. Chem. A* **2020**, *124* (9), 1867–1876. <https://doi.org/10.1021/acs.jpca.9b11981>.
- (39) Green, B. G.; Budy, S. M.; Reed, S. M.; Siemens, M. E. Measurement and Multilayer Model of Cooling of Gold Nanoparticles: Transient Thermoreflectance Experiments and Multilayer Analytical Modeling. *J. Appl. Phys.* **2018**, *124* (14), 144301. <https://doi.org/10.1063/1.5048813>.
- (40) Wilson, R. B.; Apgar, B. A.; Martin, L. W.; Cahill, D. G. Thermoreflectance of Metal Transducers for Optical Pump-Probe Studies of Thermal Properties. *Opt. Express* **2012**, *20* (27), 28829. <https://doi.org/10.1364/OE.20.028829>.
- (41) Christensen, N. E.; Seraphin, B. O. Relativistic Band Calculation and the Optical Properties of Gold. *Solid State Commun.* **1970**, *8* (15), 1221–1226. [https://doi.org/10.1016/0038-1098\(70\)90364-9](https://doi.org/10.1016/0038-1098(70)90364-9).

SUPPORTING INFORMATION
for

Nanoscale Disorder Generates Subdiffusive Heat Transport in Self-Assembled Nanocrystal Films

James K. Utterback,¹ Aditya Sood,² Igor Coropceanu,³ Burak Guzelturk,^{2,4,†} Dmitri V. Talapin,³
Aaron M. Lindenberg,^{2,4,5,6,7} Naomi S. Ginsberg^{1,8,9,10,11*}

Author Addresses

¹ Department of Chemistry, University of California, Berkeley, California 94720, United States

² Stanford Institute for Materials and Energy Sciences, SLAC National Accelerator Laboratory, Menlo Park, California 94025, United States

³ Department of Chemistry and James Franck Institute, University of Chicago, Chicago, Illinois 60637, United States

⁴ Department of Materials Science and Engineering, Stanford University, Stanford, CA 94305, United States

⁵ The PULSE Institute for Ultrafast Energy Science, SLAC National Accelerator Laboratory, Menlo Park, California 94025, United States

⁶ Department of Photon Science, Stanford University, Menlo Park, California 94025, United States

⁷ SLAC National Accelerator Laboratory, Menlo Park, California 94025, United States

⁸ STROBE, National Science Foundation Science and Technology Center, University of California Berkeley, Berkeley, California 94720, United States

⁹ Department of Physics, University of California Berkeley, Berkeley, California 94720, United States

¹⁰ Materials Science Division and Molecular Biophysics and Integrated Bioimaging Division, Lawrence Berkeley National Laboratory, Berkeley, California 94720, United States

¹¹ Kavli Energy NanoSciences Institute at Berkeley, Berkeley, California 94720, United States

† Present Address: X-ray Science Division, Argonne National Laboratory, Lemont, IL 60439, United States

*Correspondence to: nsginsberg@berkeley.edu

Methods

Sample Preparation. Spherical Au NCs with average diameters of 4.4 and 5.7 nm were prepared based on a previously described protocol with oleylamine as the native ligand.¹ The particles were gently precipitated using ethanol and then redispersed in toluene at a concentration of 20 mg/mL. Ligand exchange to DDT was performed by adding an excess of DDT to this solution followed by stirring for 15 min at room temperature. The Au NCs were then precipitated with ethanol and redispersed in toluene. Films used for stroboSCAT measurements were deposited in a N₂ atmosphere by placing a 10 μ L drop of 10 mg/mL solution of Au NCs in toluene on a 24 \times 50 mm VWR #1.5 glass coverslip and allowing it to dry at 1 atm. Glass substrates were cleaned by 10 min sonication in acetone, followed by 10 min sonication in isopropyl alcohol, then immediately dried under a flow of filtered nitrogen, and finally cleaned with an O₂ plasma for 3 min in a reactive ion etch chamber.

The sputtered Au film was fabricated at the Biomolecular Nanotechnology Center at UC Berkeley. The Au film was achieved on a DC magnetron sputter gun with argon gas with a rotating substrate holder. The deposition rate was 61 $\text{\AA}/\text{s}$ for a duration of 1 s. The deposition power was 406 Watts at a sputter current of 0.4 amps. The chamber partial pressure with argon was 20 millitorr achieved at 0.04–0.05 sccm.

Transmission Electron Microscopy. TEM micrographs were recorded on an FEI Technai F30 microscope operating at 300 kV on a graphitic carbon substrate from Ted Pella.

Atomic Force Microscopy. AFM of the films used for stroboSCAT was performed using an MFP-3D-BIO (Asylum Research) equipped with a BudgetSensors aluminum reflex coated silicon AFM probe Tap150AL-G-50 (Ted Pella, Inc.), and images were collected with 512 \times 512 pixels at a scan rate of 0.5 lines per second in tapping mode. Film thickness was determined by comparing relative heights of the position of interest, correlated to the pump-off optical scattering image of the corresponding region, to a fiducial mark, made with a razor blade, within the same image. Reported film thickness correspond to the average and standard deviation over an area that was approximately twice the pump spot size of 590 nm FWHM.

stroboSCAT Measurements. The experimental setup for stroboSCAT measurements has been previously described in detail.² Briefly, two laser diodes were used for the pump (LDH-D-C-405, PicoQuant) and the probe (LDH-D-C-640, PicoQuant) with center wavelengths of 405 and 635 nm, respectively, which were controlled by a laser driver (PDL 828-S “SEPIA II” equipped with two SLM 828 driver modules and a SOM 828-D oscillator, PicoQuant). We used a laser repetition rate of 2 MHz, with the pump modulated at 660 Hz, while the pump–probe delay times were controlled electronically using the driver with 20 ps resolution. Both pump and probe were spatially filtered through 25 μ m pinholes. The pump beam was telescoped to a \sim 6 mm diameter, while the probe beam was telescoped to 1 mm and focused into the back focal plane of the objective of a home-built microscope using an $f = 300$ mm wide-field lens. The two beams were combined using a long-pass filter (DMLP505, Thorlabs), and a 50/50 beamsplitter reflected both beams into a high numerical aperture (1.4 NA) oil-immersion objective (Leica HC PL APO 63 \times /1.40 NA) and onto the sample, resulting in an overlapped confocal pump and wide-field probe illumination, respectively. Probe light reflected from the sample–substrate interface as well as scattered from the sample are collected through the same objective; the probe light is isolated with a long-pass filter (FEL550, Thorlabs) and focused onto a charged metal oxide semiconductor (CMOS) detector

with 5.86 μm square pixels triggered at 660 Hz (PixeLINK PL-D752, equipped with a Sony IMX 174 global shutter sensor) using an $f = 500$ mm lens placed one tube length (200 mm) away from the back focal plane of the objective. The total magnification is $63 \times 500/200 = 157.5$, giving 37.2 nm/pixel. stoboSCAT images are generated by taking the difference between pump-on and pump-off raw pixel intensities, normalized to the raw pump-off intensities, yielding $\Delta R/R$ contrast images. Averaged pump-off images are simultaneously recorded at each time delay. Setup automation and data acquisition are implemented in LabVIEW 2014 64-bit. Data analysis and plotting is performed using a combination of ImageJ (Fiji),³ MATLAB, and Igor Pro. Experiments were conducted at 295 K. The 4.4 and 5.7 nm Au NC films were excited with 2σ -integrated fluences of 9 and 6 $\mu\text{J}/\text{cm}^2$, respectively. The pump powers were chosen to be in a regime where the spatially integrated signal decay was independent of pump power.

COMSOL Simulations. COMSOL Multiphysics® 5.5 (COMSOL Inc., Los Angeles, CA) finite element software was used to simulate heat transport in our NC films. The simulations were conducted using the built-in Heat Transfer in Solids module. We model Au–DDT NCs as 5.7 nm diameter Au circles with 1.8 nm thick ligand shells, with a ligand density based on calculated NC surface coverage.⁴ Custom material properties were specified. Au NC cores were given the properties of bulk Au: a density of 19,300 kg m^{-3} , thermal conductivity of 310 $\text{W m}^{-1} \text{K}^{-1}$, and heat capacity of 129 $\text{J kg}^{-1} \text{K}^{-1}$. DDT was given a density of 281 kg m^{-3} , thermal conductivity of 0.13 $\text{W m}^{-1} \text{K}^{-1}$, and heat capacity of 2043 $\text{J kg}^{-1} \text{K}^{-1}$.⁴⁻⁷ The ligand density employed was determined by assuming faceted NCs, by taking an average over the full volume occupied by a given NC’s ligand shell, and by assuming incomplete space filling between NC cores to reflect a disordered film. It is also consistent with the lower end of densities reported in the literature.⁴⁻⁷ Simulation geometries constructed starting with a 2D hexagonal lattice with center-to-center distances of $\langle d \rangle = 7.5$ nm, then voids were made by deleting NCs and their ligand shells based on the TEM image of Figure 2a, then local site disorder in NC center positions was achieved by making random displacements in the x- and y-directions were drawn from a Gaussian distribution characterized by σ_d . The Gaussian-distributed NC–NC distances within the non-void regions of Figure 2b reflect the characteristics of the local disorder in Figure 2a with inter-NC separations of $\langle d \rangle \pm \sigma_d = 7.5 \pm 1.0$ nm ($\sigma_d/\langle d \rangle = 13\%$) for each dimension of the simulation. Overlapping ligand regions (invisible in TEM) were then merged into one effective ligand component such that densities are not additive. The Au–DDT interface is treated as an equivalent thin resistive layer with a layer conductance of 600 $\text{MW m}^{-2} \text{K}^{-1}$.^{4,8} Heat transport through the voids, experimentally composed of air, is neglected. The boundaries of the simulation geometry are insulated from the environment. 300 K was used as the ambient reference temperature, and simulations are initialized using a Gaussian profile (FWHM = 76 nm) of elevated temperature with a peak of 301 K ($\Delta T_{\text{max}} = 1$ K) in the Au NC cores in Figure 2, or with only the central NC elevated to 301 K in Figure 3. The mesh was constructed using triangular elements. The finite element simulation solves the heat equation using a quadratic Lagrange discretization to calculate the time dependence of the temperature profile with a relative tolerance of 0.0001.

The simulated temperature profiles as a function of time were treated analogously to the stoboSCAT data, taking a 360° azimuthal profile average in ImageJ, fitting to a Gaussian function over time, and calculating $\sigma^2(t) - \sigma^2(0)$ to produce mean-squared expansion curves (Figure 2d). The geodesic map was calculated from the center of the central NC of the simulation geometry, using ImageJ using the MorphoLibJ plugin package.³

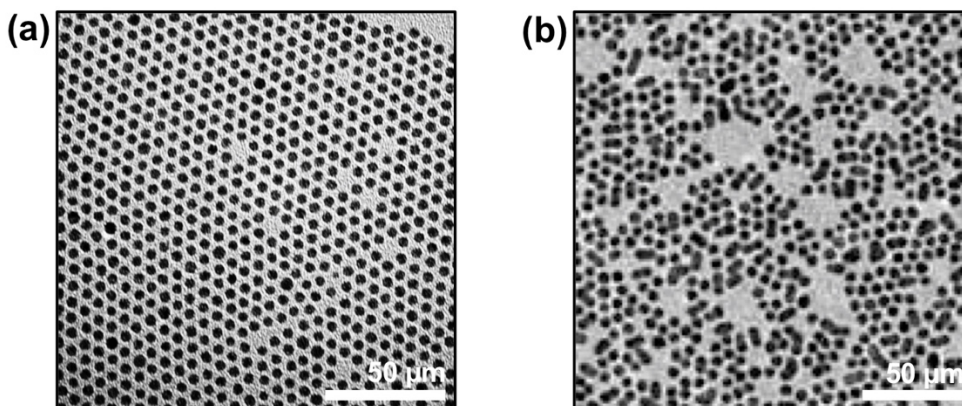


Figure S1. TEM images of (a) 4.4 and (b) 5.7 nm diameter Au NCs used in this manuscript.

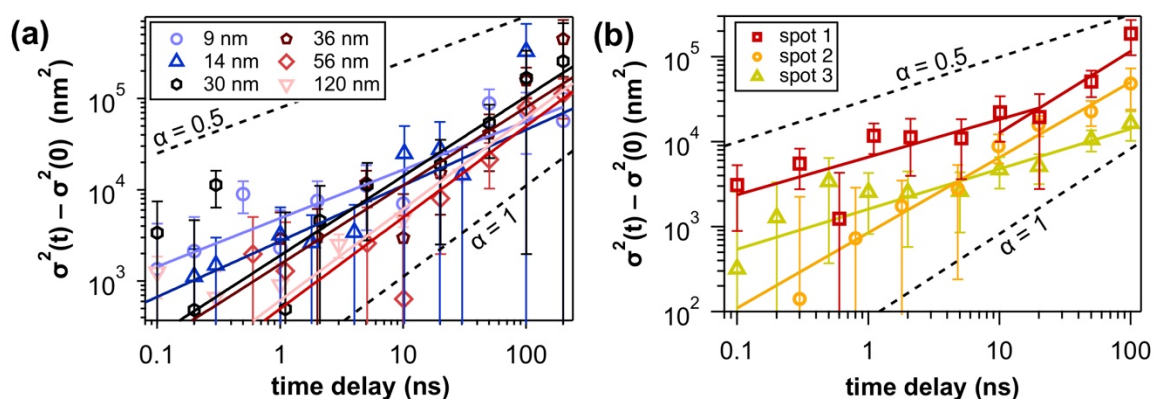


Figure S2. (a) Mean-squared expansion curves for 4.4 nm Au-DDT NC films as a function of film thickness. Fitted values of α appear in Figure 1d. (b) Representative mean-squared expansion curves for several regions within the 5.7 nm Au-DDT NC film, where α ranges from 0.42 to ~ 1 in different regions of the film. Spot 1 has $\alpha = 0.45 \pm 0.08$ when fit over 0.1–20 ns, and $\alpha = 0.97 \pm 0.09$ for 10–100 ns. Spot 2 has $\alpha = 0.78 \pm 0.16$ over 0.1–100 ns. Spot 3 has $\alpha = 0.42 \pm 0.11$ over 0.1–100 ns.

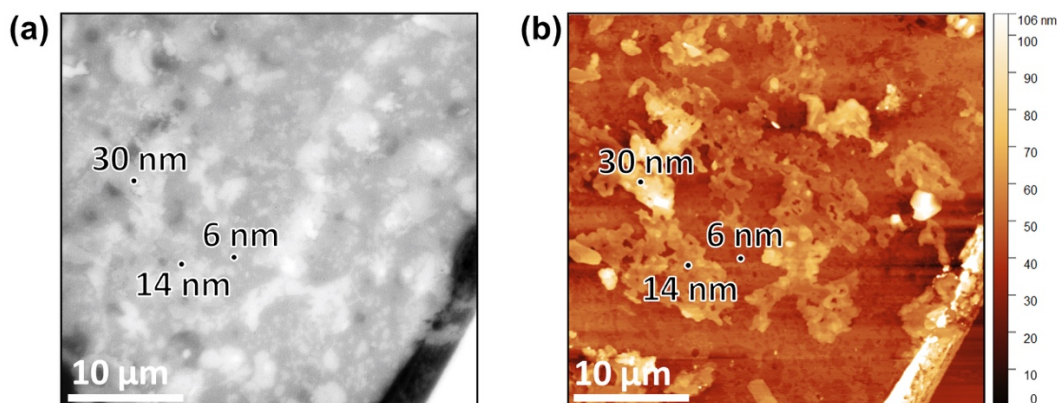


Figure S3. Representative (a) pump-off optical scattering and (b) AFM images of a 4.4 nm gold NC film with DDT ligands from correlated stroboSCAT and AFM. Regions probed using stroboSCAT corresponding to data in Figure 1d and S2 are highlighted with circles to scale for a 590 nm pump spot size.

Thermal diffusivity and conductivity

To find a representative heat diffusion coefficient of the Au NC films studied here, the mean-squared expansion curve of the 120-nm-thick region in Figure 1c was fit to the function $\sigma^2(t) - \sigma^2(0) = 2Dt$ over the 3–100 ns time window where $\alpha \sim 1$, giving a heat diffusion coefficient of $D = (3.0 \pm 0.2) \times 10^{-3} \text{ cm}^2 \text{ s}^{-1}$. We estimated the corresponding thermal conductivity, k , by calculating $k = D\rho C_p$, where ρ is the volume fraction-weighted density of the composite medium and C_p is the mass-weighted specific heat capacity.⁹ The volume fraction of the 4.4 nm Au–DDT film was estimated from Figure S1a to be 0.23, and the density and heat capacity values used for the simulations (Methods) were used to give an approximate value of k of $0.3 \text{ W m}^{-1} \text{ K}^{-1}$, consistent with previous literature values.⁹

Treating the mean-squared expansion curve of the ~ 6 nm thick sputtered Au film (Figure S4) in the same manner as above gives $D = (1.1 \pm 0.1) \times 10^{-1} \text{ cm}^2 \text{ s}^{-1}$ and $k = 27 \pm 2 \text{ W m}^{-1} \text{ K}^{-1}$, consistent with being an ultra-thin polycrystalline film.^{10,11}

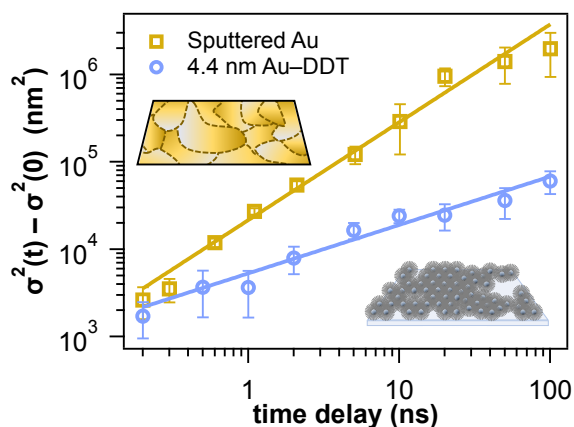


Figure S4. Control experiment showing normal heat diffusion in a ~ 6 nm thick polycrystalline Au film compared to 4.4 nm Au–DDT NC film.

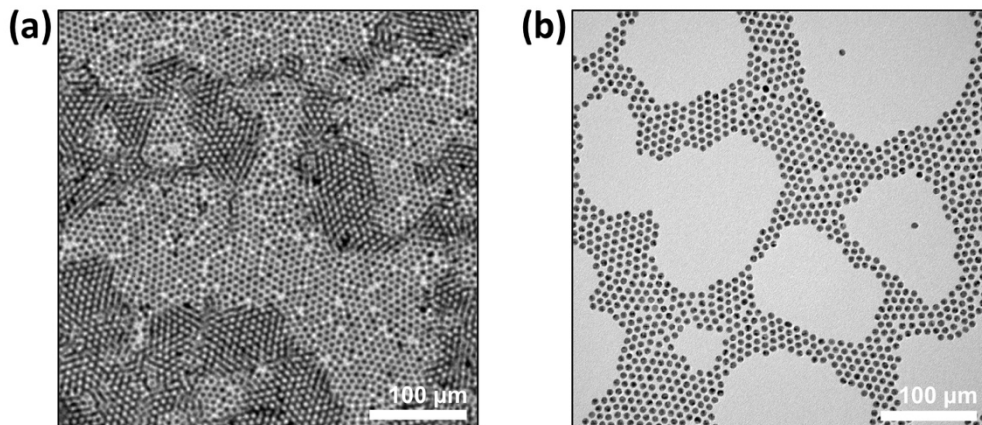


Figure S5. TEM image of (a) multilayer compared to (b) submonolayer film of Au NCs with DDT ligands.

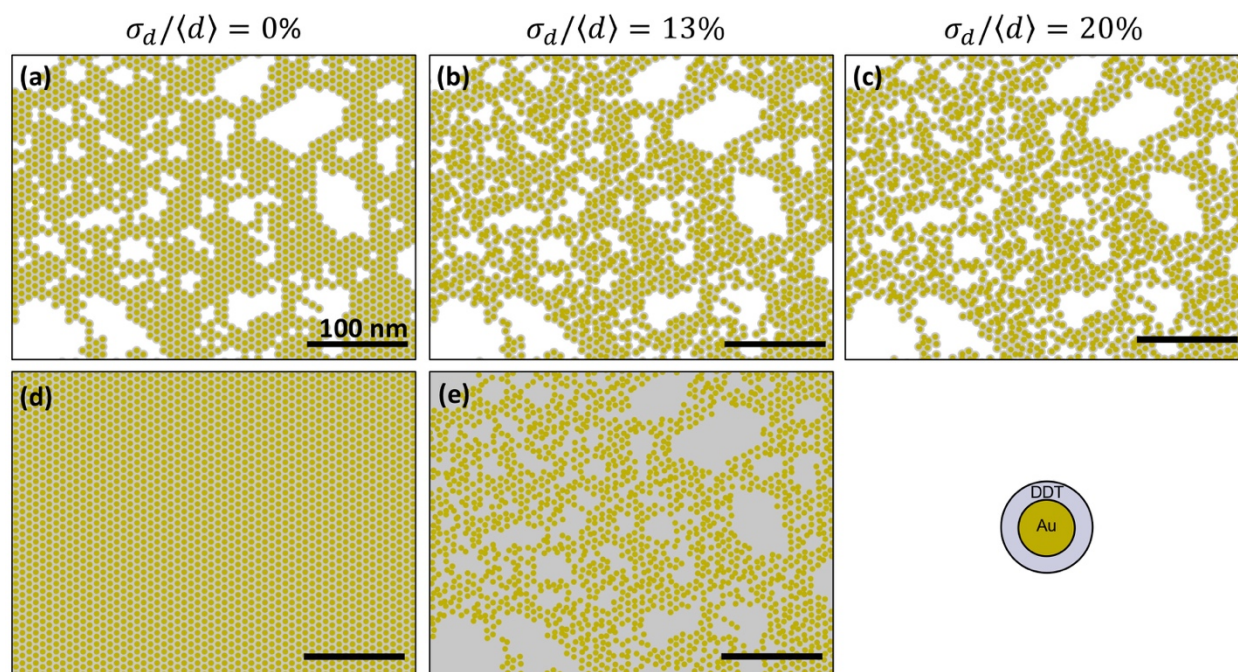


Figure S6. Simulation geometries. TEM-based voids with local displacements of (a) $\sigma_d/\langle d \rangle = 0$, (b) $\sigma_d/\langle d \rangle = 13\%$ and (c) $\sigma_d/\langle d \rangle = 20\%$. (d) No voids and local order $\sigma_d/\langle d \rangle = 0$. (e) Same geometry as in (b) but voids filled with ligand. Scale bar (black) is 100 nm in all panels.

Heat Transport Simulation Results

Figure S7 shows the simulated temperature maps over time for additional simulation geometries not presented in the main text. Within 100 ps of the initial temperature elevation in the Au NC cores—the experimental pulse duration—heat has transferred through the Au–DDT interface and the temperature profile within each individual NC is uniform due to fast heat conduction (Figure S8); the only gradients in the film are found in the more weakly conducting interstitial ligand material between nearest, connected NC neighbors. Beyond 100 ps, the granularity of the composite materials is apparent yet small compared to the length scale of the profile.

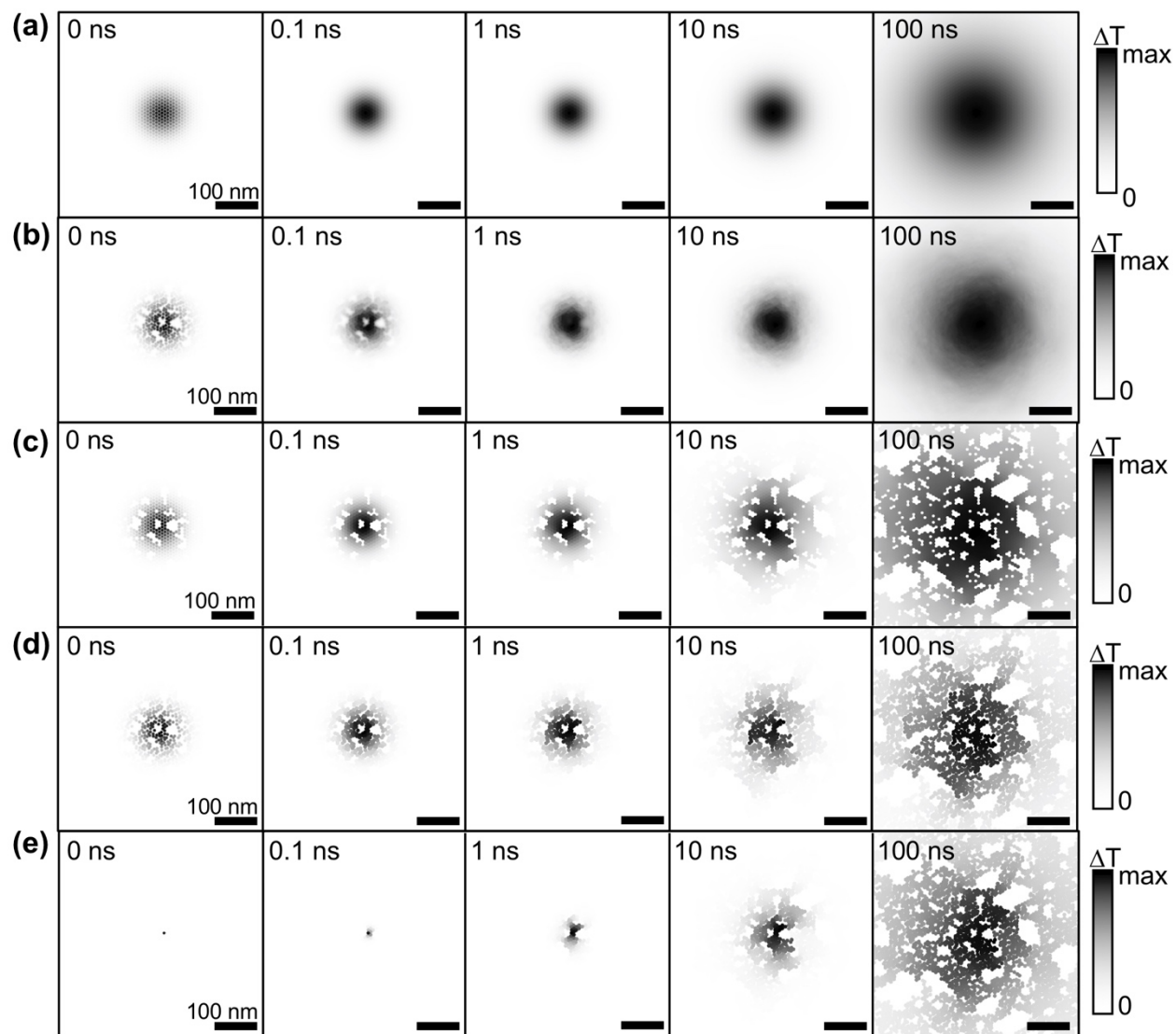


Figure S7. Simulated temperature maps over time for additional geometries that may be directly compared with Figure 2c. (a) Ordered NC array with no voids and $\sigma_d/\langle d \rangle = 0$. (b) Voids filled in the ligand material and $\sigma_d/\langle d \rangle = 13\%$. (c) Film with voids and $\sigma_d/\langle d \rangle = 0$. (d) Film with voids and $\sigma_d/\langle d \rangle = 20\%$. Figure panels (a)-(d) used a Gaussian profile (FWHM = 76 nm) of elevated temperature with a peak of $\Delta T = 1$ K in the Au NC cores. The corresponding radial mean-squared expansion curves (Figure 2d,e) were constructed by azimuthal averaging fitting the temperature profiles to a Gaussian function over time. (e) Geometry of Figure 2b with voids present and $\sigma_d/\langle d \rangle = 13\%$, but with initial temperature of only the central NC core raised to $\Delta T = 1$ K.

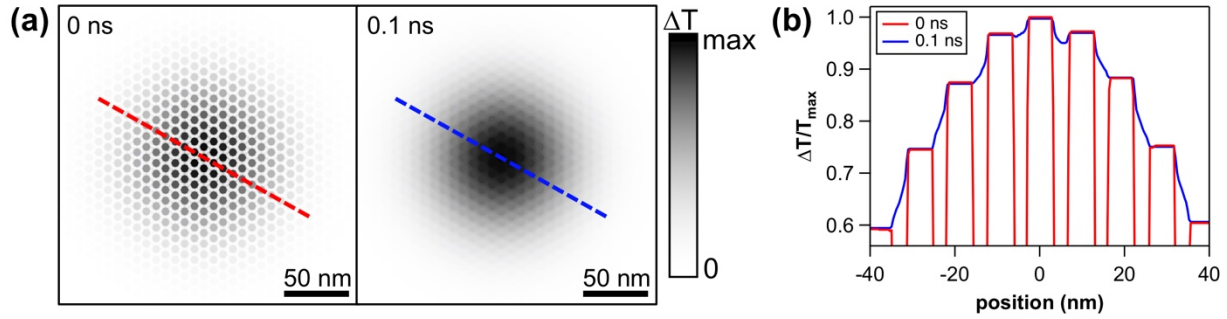


Figure S8. NC-to-ligand heat transfer. (a) Close-ups of simulated temperature maps of the ordered NC array from Figure S7a at 0 and 0.1 ns. (b) Temperature profiles of the corresponding line cuts in (a).

Determination of $\langle \ell_{\min}^2 \rangle$

We determined the mean-squared expansion in geodesic space, $\langle \ell_{\min}^2 \rangle$, found in Figure 3c for the simulation geometry with voids and $\sigma_d/\langle d \rangle = 13\%$ in the following manner. We compared the geodesic distance map (Figure 3a) and simulated time-dependent temperature maps (Figure S7e) to map the temperature onto the associated geodesic distance as a function of time, placing a point on the $\ell_{\min} - \Delta T/T_{\max}$ space scatter plot in Figure S9a for each simulation grid point at each of the simulation times indicated in the legend. In order to directly compare geodesic distance and simulated temperature maps, it was necessary to use the initial conditions of raising the temperature of only the single central NC rather than the broader initial profile in Figure 2c that is more representative of the finite-sized pump laser excitation because the geodesic distance is measured from a single point. We then found the half width at half max (HWHM) of the resulting temperature profiles, and calculated $\text{HWHM}^2(t) - \text{HWHM}^2(0)$ to produce the mean-squared expansion curve in Figure 3c. We chose to use a HWHM analysis here because the initial temperature profile is not Gaussian, though the profiles become consistent with Gaussian functions as time progresses.

To provide more intuition for the comparison of the expansion of the temperature profile over time and the geodesic distance, Figure S9b and c respectively compare contour plots of the average geodesic distance corresponding to $\Delta T/T_{\max} = 1/2$ (the temperature corresponding to $\ell_{\min} = \text{HWHM}$) and the $\Delta T/T_{\max} = 1/2$ contour of the simulated temperature profile as a function of time. The average radial distance of the contours at each time point are approximately equal in the two plots, but variations occur due to heat moving through the composite medium containing two drastically different thermal diffusivities and interfacial resistance that cause isothermal contours to bend around the Au NC cores.

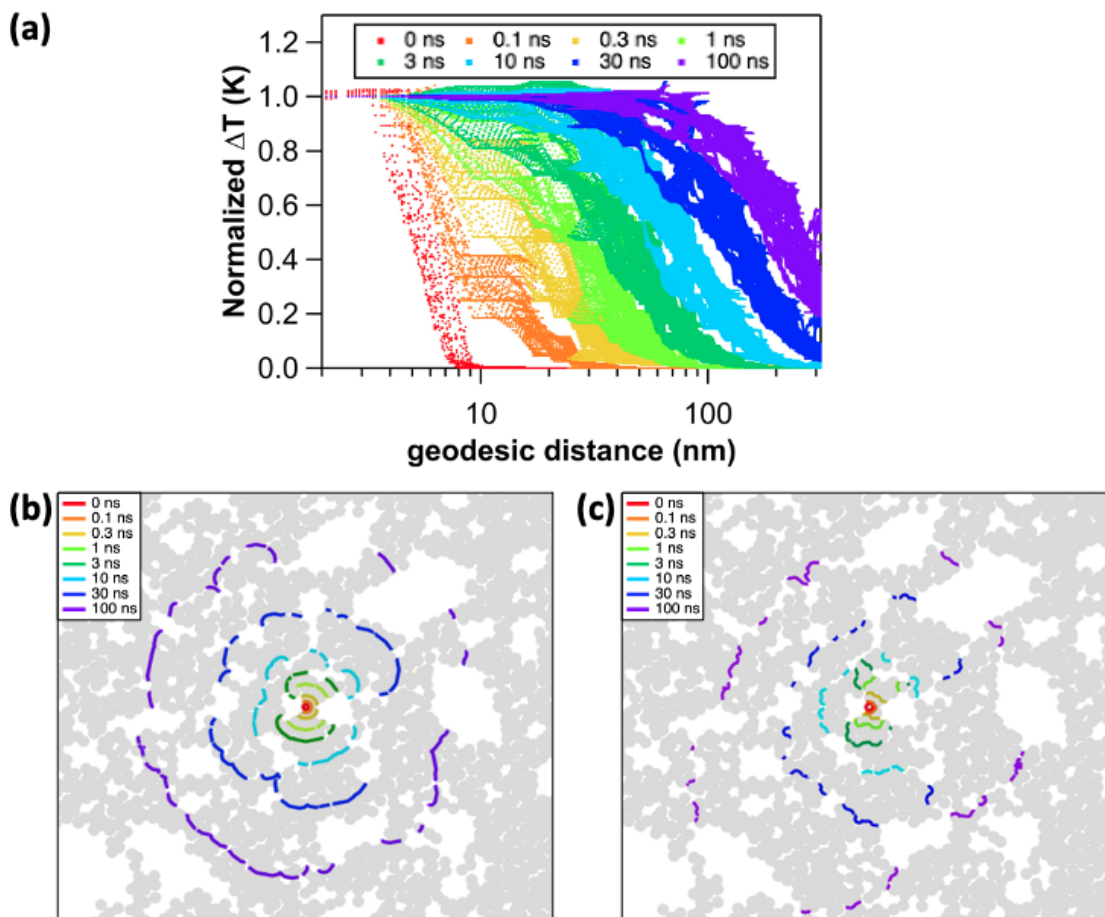


Figure S9. (a) Scatter plots yield the one-dimensional temperature profile versus geodesic distance over time after raising the temperature of the central NC by $\Delta T = 1$ K, obtained by mapping the simulated temperature profile from Figure S7e onto the geodesic distance from Figure 3a at each grid point. (b) Contour map of the average geodesic distance corresponding to $\Delta T/T_{\max} = 1/2$ as a function of time. (c) Expansion of the $\Delta T/T_{\max} = 1/2$ contour of the temperature profile as a function of time after raising the temperature of the central NC by $\Delta T = 1$ K. All panels feature the TEM-inspired geometry with voids and $\sigma_d/\langle d \rangle = 13\%$ from Figure 2a.

Correlation between voids, geodesic distance and instantaneous subdiffusive exponent

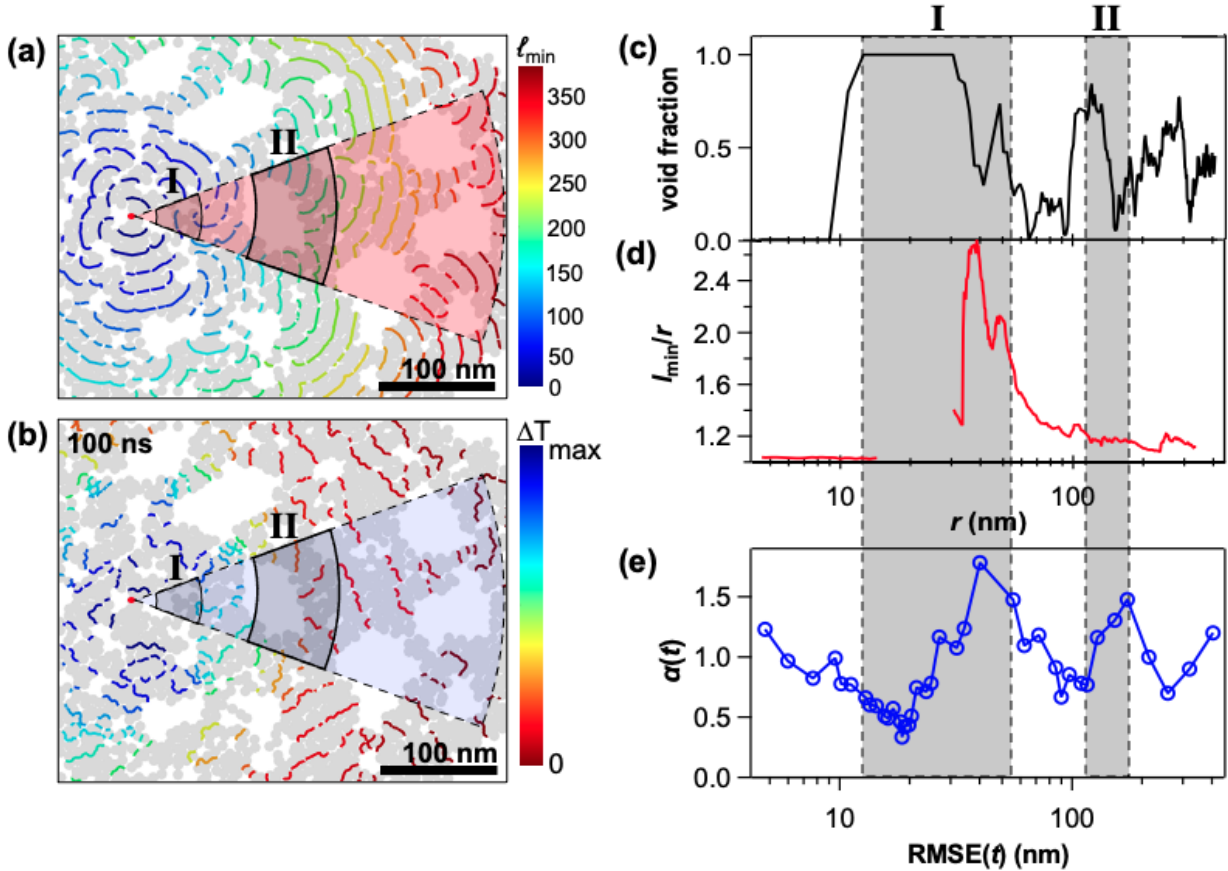


Figure S10. (a) Contour maps of the geodesic distance from the central NC in nm and (b) the temperature 100 ns after raising the temperature of the central NC by $\Delta T = 1$ K for TEM-inspired geometry with voids and $\sigma_d/\langle d \rangle = 13\%$. The colored wedges show the regions integrated to obtain the void fraction, ℓ_{\min}/r , and the mean-squared expansion used to find α . (c) Area fraction of the voids as a function of radial distance, averaged over the wedge shown in (a). (d) ℓ_{\min}/r as a function of radial distance, averaged over the wedge shown in (a). (e) Parametric plot of the azimuthally averaged instantaneous subdiffusive exponent $\alpha(t)$ as a function of the root-mean-squared expansion $\text{RMSE}(t)$ for the wedge indicated in (b).

In order to further relate the correspondence of the geodesic and temperature maps of Figure 3 to subdiffusivity, we show that decreases in α are correlated with encountering voids and increases in ℓ_{\min} . Figure S10a,b shows the geodesic distance map and the temperature map at 100 ns for an initial condition in which only the central NC is elevated to $\Delta T = 1$ K (Figure S7e). Regions I and II highlight representative regions where the contours curve radially inwards on the far sides of voids. These maps were plotted from the same data as in Figure 3a,b of the main text, only showing a region of interest that highlights the correlations discussed herein. Within the radial wedge highlighted in Figure S10a, we calculated the area fraction of the voids (Figure S10c) as well as the ratio ℓ_{\min}/r (Figure S10d) as function of r . Consistent with the geodesic distance contour map, increases in ℓ_{\min} relative to r occur on the far side of voids because the geodesic distance has to circumnavigate the voids to get there. Finally, we developed another metric whose radial dependence also strongly correlates to those of the void fraction and geodesic distance: we found the instantaneous subdiffusive exponent as a function of time, $\alpha(t)$, by taking the derivative of the

azimuthally averaged mean-squared expansion of heat within the radial wedge indicated in Figure S10b. Because $\alpha(t)$ cannot be plotted against r directly, we calculated the root-mean-squared expansion as a function of time, $\text{RMSE}(t) = \sqrt{[\sigma^2(t) - \sigma^2(0)]}$, since it provides a length scale that can also be related to time delay t . We then made a parametric plot of $\alpha(t)$ against $\text{RMSE}(t)$ (Figure S10e) that could be directly compared to the respective plots of the void fraction and of ℓ_{\min}/r against r (Figure S10c,d). Together, Figures S10c-e show that the positions of the voids show some degree of correlation to decreases in $\alpha(t)$, and some degree of anticorrelation to spikes in the geodesic distance; likewise, increases in $\alpha(t)$ are somewhat correlated to spikes in the geodesic distance. The shaded regions I and II in the radial plots are representative examples that highlight transitions from within a void to the far side of voids (Figure S10c) over which ℓ_{\min} increases (Figure S10d) and where α returns towards ~ 1 after being < 1 (Figure S10e). We note that the average value of α for this wedge and initial condition over the 0.1–100 ns time window is 0.70, differing from the value of 0.80 found with a larger initial temperature profile and complete azimuthal averaging (Figure 2d), which shows that the degree of subdiffusivity varies within regions of the film.

References

1. Yang, Y.; Wang, B.; Shen, X.; Yao, L.; Wang, L.; Chen, X.; Xie, S.; Li, T.; Hu, J.; Yang, D.; Dong, A. Scalable Assembly of Crystalline Binary Nanocrystal Superparticles and Their Enhanced Magnetic and Electrochemical Properties. *J. Am. Chem. Soc.* **2018**, *140* (44), 15038–15047.
2. Delor, M.; Weaver, H. L.; Yu, Q.; Ginsberg, N. S. Imaging Material Functionality through Three-Dimensional Nanoscale Tracking of Energy Flow. *Nat. Mater.* **2020**, *19* (1), 56–62.
3. Schneider, C. A.; Rasband, W. S.; Eliceiri, K. W. NIH Image to ImageJ: 25 Years of Image Analysis. *Nat. Methods* **2012**, *9* (7), 671–675.
4. Ong, W.-L.; Majumdar, S.; Malen, J. A.; McGaughey, A. J. H. Coupling of Organic and Inorganic Vibrational States and Their Thermal Transport in Nanocrystal Arrays. *J. Phys. Chem. C* **2014**, *118* (14), 7288–7295.
5. Waltmann, C.; Horst, N.; Travasset, A. Potential of Mean Force for Two Nanocrystals: Core Geometry and Size, Hydrocarbon Unsaturation, and Universality with Respect to the Force Field. *J. Chem. Phys.* **2018**, *149* (3), 034109.
6. Boles, M. A.; Talapin, D. V. Many-Body Effects in Nanocrystal Superlattices: Departure from Sphere Packing Explains Stability of Binary Phases. *J. Am. Chem. Soc.* **2015**, *137* (13), 4494–4502.
7. Torelli, M. D.; Putans, R. A.; Tan, Y.; Lohse, S. E.; Murphy, C. J.; Hamers, R. J. Quantitative Determination of Ligand Densities on Nanomaterials by X-Ray Photoelectron Spectroscopy. *ACS Appl. Mater. Interfaces* **2015**, *7* (3), 1720–1725.
8. Guzelturk, B.; Utterback, J. K.; Coropceanu, I.; Kamysbayev, V.; Janke, E. M.; Zajac, M.; Yazdani, N.; Cotts, B. L.; Park, S.; Sood, A.; Lin, M.-F.; Reid, A. H.; Kozina, M. E.; Shen, X.; Weathersby, S. P.; Wood, V.; Salleo, A.; Wang, X.; Talapin, D. V.; Ginsberg, N. S.; Lindenberg, A. M. Nonequilibrium Thermodynamics of Colloidal Gold Nanocrystals Monitored by Ultrafast Electron Diffraction and Optical Scattering Microscopy. *ACS Nano* **2020**, *14* (4), 4792–4804.
9. Ong, W.-L.; Rupich, S. M.; Talapin, D. V.; McGaughey, A. J. H.; Malen, J. A. Surface Chemistry Mediates Thermal Transport in Three-Dimensional Nanocrystal Arrays. *Nat. Mater.* **2013**, *12*(5), 410415.
10. Lin, H.; Xu, S.; Li, C.; Dong, H.; Wang, X. Thermal and Electrical Conduction in 6.4 nm Thin Gold Films. *Nanoscale* **2013**, *5* (11), 4652.
11. Mason, S. J.; Wesenberg, D. J.; Hojem, A.; Manno, M.; Leighton, C.; Zink, B. L. Violation of the Wiedemann-Franz Law through Reduction of Thermal Conductivity in Gold Thin Films. *Phys. Rev. Mater.* **2020**, *4* (6), 065003.